PHYSICAL REVIEW A **89**, 062503 (2014)

Detection of barium 6*sng* → 6*snh*, 6*sni*, and 6*snk* microwave transitions using selective excitation to autoionizing states

E. G. Kim,[1] J. Nunkaew,[2,*] and T. F. Gallagher[1]

[1]*Department of Physics, University of Virginia, Charlottesville, Virginia 22904, USA*

[2]*Department of Physics and Materials Science, Faculty of Science, Chiang Mai University, Chiang Mai 50200, Thailand*

(Received 4 October 2013; revised manuscript received 9 April 2014; published 5 June 2014)

We use selective laser excitation to an autoionizing state to observe the microwave transitions of Ba from the $6sng$ Rydberg states to the $6snh$, $6sni$, and $6snk$ states for $15 \leqslant n \leqslant 18$. We extract the dipole and quadrupole polarizabilities of Ba$^+$ from the measured $\Delta\ell$ intervals of the Ba $6sn\ell$ states of $\ell \geqslant 5$ using a nonadiabatic core polarization model. The values we determine for the dipole and quadrupole polarizabilities are $\alpha_d = 124.81(25)a_0^3$ and $\alpha_q = 2478(50)a_0^5$, respectively.

DOI: 10.1103/PhysRevA.89.062503 PACS number(s): 32.10.Dk, 32.80.Zb, 32.80.Ee

I. INTRODUCTION

One of the largest frequency shifts in present-day atomic clocks is the blackbody radiation shift [1–4]. Since 300 K blackbody radiation is low in frequency, the blackbody shift is predominantly determined by the static polarizability of the atom or ion used in the clock. For many alkaline-earth-metal ions used in atomic clocks, there are no measurements of the ionic dipole and quadrupole polarizabilities to serve as benchmarks for calculations of the blackbody shifts. It is possible to extract these polarizabilities from the intervals between high-ℓ Rydberg states of the atom, states of high enough ℓ that the Rydberg electron does not penetrate the ionic core [5–8]. We follow the usual convention that n and ℓ are the principal and orbital angular momentum quantum numbers of the Rydberg electron. In these nonpenetrating states, the energy shifts from the hydrogenic levels arise from polarization of the core by the field from the Rydberg electron. In Rydberg states of lower ℓ, the electron comes closer to the core at the inner turning point of its orbit, and the energy shift is larger. Thus, measuring the $\Delta\ell$ intervals yields the polarizabilities of the ionic core. An excellent recent summary of core polarization analysis has been given by Lundeen [8].

Several methods have been employed to detect transitions between the high-ℓ states of alkaline-earth-metal atoms. Selective field ionization has been used by Gentile *et al.* to measure the $4sn\ell$ intervals in Ca [9]. Gallagher *et al.* and Nunkaew *et al.* have used delayed field ionization to detect the Ba $6sn\ell$ and Sr $5sn\ell$ intervals [10,11]. Snow and Lundeen have used resonant excitation Stark ionization spectroscopy (RESIS) to measure the Ba $6sn\ell$ and Mg $3sn\ell$ intervals [12,13]. Field ionization is useful for states of $n \sim 20$, and RESIS can be used for states which can be populated by driving transitions from $n = 9$ and 10 using a CO$_2$ laser. Here we point out that the optical excitation to an autoionizing state by isolated core excitation (ICE) can be used to detect $\Delta\ell$ intervals of alkaline-earth-metal atoms over a much wider range of n [14]. The basis of this notion is that the rapid increase in the ICE cross section with ℓ allows the microwave $\Delta\ell$ transitions between the bound states to be detected, even when the ICE transitions for different ℓ states occur at essentially the same wavelength. Here we report the use of this technique to measure the Ba $6sng$-$6snh$-$6sni$-$6snk$ intervals for $15 \leqslant n \leqslant 18$. This technique should be applicable for all Ba states of $n \leqslant 30$.

II. THE MICROWAVE $\Delta\ell$ TRANSITIONS AND THEIR DETECTION USING ICE

The $\Delta\ell$ microwave transitions we observe are shown in Fig. 1. The $6sng$ $^1G_4$ state is populated by laser excitation, and we drive the microwave transitions to the $6sn\ell$ states of $5 \leqslant \ell \leqslant 7$. The higher-$\ell$ states are not singlets and triplets. Rather, the total angular momentum of the core $\vec{j}_c$ is coupled to the orbital angular momentum $\vec{\ell}$ of the Rydberg electron to form $\vec{K}$. Explicitly,

$$\vec{K} = \vec{j}_c + \vec{\ell}. \tag{1}$$

We ignore the spin of the Rydberg electron. Since $j_c = 1/2$, $K = \ell \pm 1/2$, and for each ℓ state we observe two transitions, as shown in Fig. 1. The splitting between the two K levels is due to the indirect spin-orbit splitting [15,16].

Detection of the Ba $6sn\ell \rightarrow 6sn\ell'$ transitions ($\ell' > \ell$) is based on the difference in the optical cross sections of the $6sn\ell \rightarrow 6p_{1/2}n\ell$ and $6sn\ell' \rightarrow 6p_{1/2}n\ell'$ ICE transitions. Previously, Cooke and Gallagher used the substantial difference in the wavelengths of the Sr $5snd \rightarrow 5pnd$ and $5snf \rightarrow 5pnf$ ICE transitions to detect the Sr $5s(n+2)d \rightarrow 5snf$ microwave transitions [17]. In ICE of the $6sn\ell$ state, the $6s$ electron absorbs the photon while the $n\ell$ electron is a spectator. The $6s \rightarrow 6p_{1/2}$ transition of the inner electron is essentially the Ba$^+$ $6s \rightarrow 6p_{1/2}$ transition, with an oscillator strength of 1/3. The oscillator strength is spread over the spectral width of the $6p_{1/2}n\ell$ state, which is determined by its autoionization rate. In this case, the peak optical cross section is given by

$$\sigma_{\text{peak}} = \frac{\lambda^2 A}{8\pi\Gamma_{n\ell}}, \tag{2}$$

where A is the Einstein A coefficient for the Ba$^+$ $6s \rightarrow 6p_{1/2}$ transition, $\Gamma_{n\ell}$ is the autoionization rate of the $6p_{1/2}n\ell$ state, and λ is the wavelength of the transition, 493.5 nm in this case. We have implicitly assumed that the autoionization rates of the $6p_{1/2}n\ell$ states exceed their radiative decay rates, which is in all cases simply the radiative decay rate of the Ba$^+$ $6p_{1/2}$ state.

---

[*] jn8h@virginia.edu

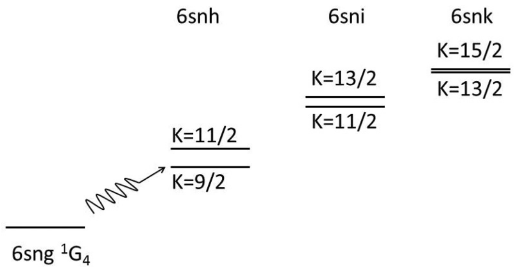

FIG. 1. The Ba $6sn\ell$, $\ell \geqslant 4$, states showing the microwave transitions and the K splittings due to the indirect spin-orbit coupling of the $6sn\ell$, $\ell \geqslant 5$, Rydberg states.

For the $6p_{1/2}n\ell$ states of interest this condition is easily met. However, for $n \geqslant 30$ the autoionization rate of a $6p_{1/2}n\ell$ state of $\ell = 7$ is less than the radiative decay rate, and this method of detection will no longer work [18].

The autoionization rates of the Ba $6p_{1/2}n\ell$ states of $\ell \geqslant 4$ decrease by roughly a factor of 5 with each increase in ℓ of 1 [19]. Accordingly, the cross section for the $6sn\ell \rightarrow 6p_{1/2}n\ell$ ICE transition increases by a factor of 5 for each increase in ℓ of 1. Even if the center frequencies of the ICE transitions are the same, approximately the ionic $6s \rightarrow 6p_{1/2}$ frequency, it is possible to observe transitions between the $6sn\ell$ and $6sn\ell'$ states, as shown in Fig. 2. Figure 2 is drawn assuming the two ICE transitions occur at the ionic frequency and that $\ell' = \ell + 1$, so the ICE cross sections and widths differ by a factor of 5. The linewidth of the laser driving the ICE transition must be less than the width of the $6p_{1/2}n\ell$ state, and the power of the laser must also be kept below saturation of the $6sn\ell' \rightarrow 6p_{1/2}n\ell'$ transition. If the laser linewidth is less than the $6p_{1/2}n\ell'$ linewidth and the $6sn\ell' \rightarrow 6p_{1/2}n\ell'$ transition is not saturated, an atom in the $6sn\ell'$ state is five times as likely as one in the $6sn\ell$ state to undergo the ICE transition when the ICE laser is tuned to the peak of the cross sections, at the ionic frequency. In short, with the ICE laser tuned to the peak of the cross sections, driving the $6sn\ell \rightarrow 6sn\ell'$ microwave transition can result in a fivefold increase in the autoionization signal at the $6sn\ell$-$6sn\ell'$ microwave resonance. Alternatively, the ICE laser can be tuned to the wing of the $6sn\ell \rightarrow 6p_{1/2}n\ell$ transition, in which case the microwave $6sn\ell \rightarrow 6sn\ell'$ transition results in a decrease in the autoionization signal.

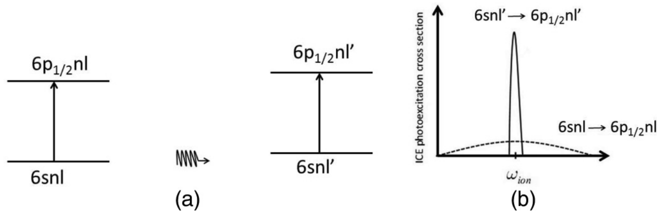

FIG. 2. (a) The $6sn\ell \rightarrow 6sn\ell'$ microwave transition can be detected using the difference in the two ICE cross sections. (b) The ICE cross sections of the $6sn\ell \rightarrow 6p_{1/2}n\ell$ and $6sn\ell' \rightarrow 6p_{1/2}n\ell'$ transitions. With the ICE laser tuned to the peak of the cross sections, driving the $6sn\ell \rightarrow 6sn\ell'$ microwave transition can result in a fivefold increase in the autoionization signal at the $6sn\ell$-$6sn\ell'$ microwave resonance if $\ell' = \ell + 1$.

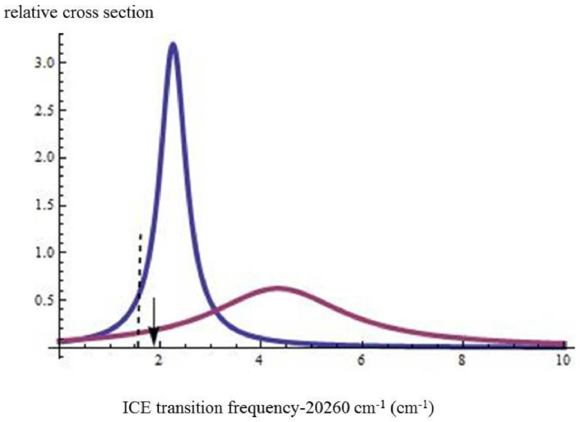

FIG. 3. (Color online) The ICE cross sections for the $6s17g$ and $6s17h$ states. The wider ICE cross section is the $6s17g \rightarrow 6p_{1/2}17g$ transition. The narrower ICE cross section is the $6s17h \rightarrow 6p_{1/2}17h$ transition. The arrow shows the location of the $6s17i \rightarrow 6p_{1/2}17i$ ICE transition. The dashed line shows the location of the ionic $6s \rightarrow 6p_{1/2}$ transition frequency.

In Ba, the $6sn\ell \rightarrow 6p_{1/2}n\ell$ transition frequencies depend on both n and ℓ. Figure 3 shows the ℓ dependence of the $6s17\ell \rightarrow 6p_{1/2}17\ell$, $\ell = 4$ and 5, ICE cross sections. We do not show the $6s17\ell \rightarrow 6p_{1/2}17\ell$ ICE cross sections for $\ell > 5$ since the peak cross sections are so much higher. We do, however, show the location of the $\ell = 6$ ICE transition. The higher-ℓ ICE transitions lie closer to the ion $6s$-$6p_{1/2}$ transition at 20 261.56 cm^{-1}. Since the $6s17g$ and $6s17h$ ICE transitions are not superimposed, at the peak of the $6s17h$ ICE transition the ratio of the cross sections is not 5, but 10. While the increased selectivity is attractive, the displacement of the ICE transitions with ℓ does complicate finding the ICE transitions for higher-ℓ states. In this case the most straightforward approach might be to set the ICE laser to the high-frequency side of the $6s17g \rightarrow 6p_{1/2}17g$ transition and look for a decrease in the autoionization signal to detect the $6s17g \rightarrow 6s17\ell$ microwave transitions. However, we have used a different approach. Since the frequencies of the transitions from the Ba $6s18g$ state to the $6s18h$, $6s18i$, and $6s18k$ states are known [10], we set the microwave frequency to the $6s18g \rightarrow 6s18\ell$ resonance and scanned the ICE laser to find the $6s18\ell \rightarrow 6p_{1/2}18\ell$ ICE transition, which occurs at the frequency ν_ℓ, given by

$$\nu_\ell = \nu_{\text{ion}} + \frac{\delta_{\ell_s} - \delta_{\ell_p}}{n^3}, \tag{3}$$

where ν_{ion} is the Ba$^+$ $6s$-$6p_{1/2}$ frequency, and δ_{ℓ_s} and δ_{ℓ_p} are the quantum defects of the $6sn\ell$ and $6p_{1/2}n\ell$ states, respectively. When n is decreased by 1 the change in the ICE frequency, $\Delta\nu_\ell$, is given by

$$\Delta\nu_\ell = 3\frac{\delta_{\ell_s} - \delta_{\ell_p}}{n^4}. \tag{4}$$

For $n = 18$ and $\ell = 5$, $\Delta\nu_\ell = 2.5$ GHz, which is small compared to the 10 GHz width of the $6p_{1/2}18h$ state. In short, knowing the $\ell = 5$, 6, and 7 ICE frequencies for $n = 18$ allows us to predict them accurately enough to make the $n = 17$, 16, and 15 measurements.

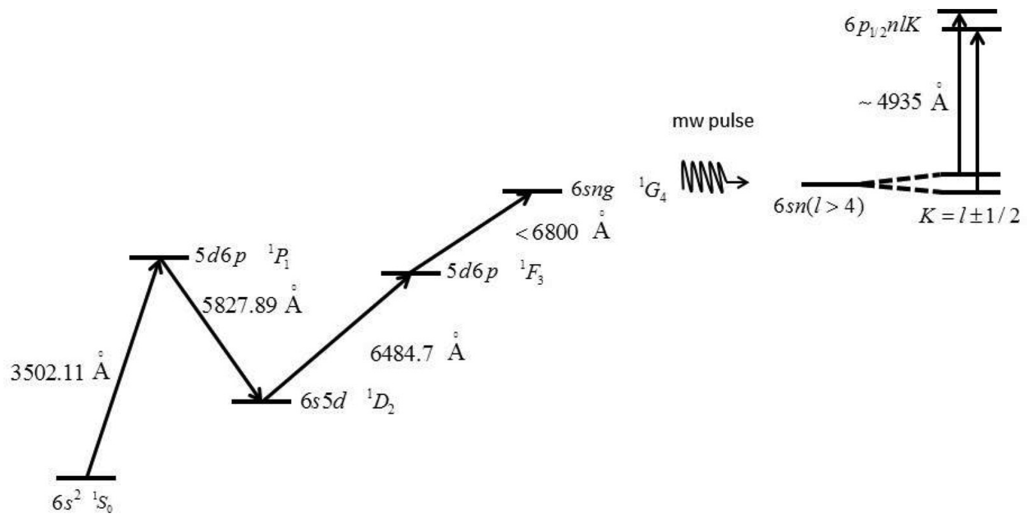

FIG. 4. Laser excitation scheme of the experiment.

III. EXPERIMENTAL APPROACH

We prepare $6sng$ barium Rydberg states by exciting neutral barium atoms in a beam with four laser pulses. The excitation scheme from the ground state $6s^2$ to the $6sng$ state is shown in Fig. 4. Photoions and electrons are produced, so the excitation is performed in a small electric field, less than 100 V/cm, to remove them.

As shown by the timing diagram of Fig. 5 after the four laser pulses, we turn off the electric field and wait 200 ns for any ringing from the electronics to dissipate. It is important that there be no stray electric field on the Rydberg atoms during the microwave pulse to avoid Stark shifts of our observed intervals. To drive the $6sng \rightarrow 6snh$ and $6sng \rightarrow 6sni$ transitions, we apply a single 1 μs pulse of microwaves; while for the $6sng \rightarrow 6snk$ transitions, we use a continuous radio-frequency (rf) field in addition to a 1 μs microwave pulse. When the microwave pulse ends, we immediately apply a ~493.5 nm frequency-doubled, dye-amplified diode laser pulse, which excites the $6sn\ell$ atoms to the autoionizing $6p_{1/2}n\ell$ states. The $6p_{1/2}n\ell$ atoms autoionize quickly, and we apply an electric field ramp to drive the resulting ions to the microchannel plate detector. The peak of the field ramp is high enough to ionize bound $6sn\ell$ atoms of $n > 16$, but the signal from bound-state atoms arrives 1 μs later than the signal from autoionizing atoms. The two signals are temporally well resolved, and we set the gate of the gated integrator on the autoionization signal. This excitation and detection cycle is repeated every 50 ms, and our signals are averaged over many laser shots.

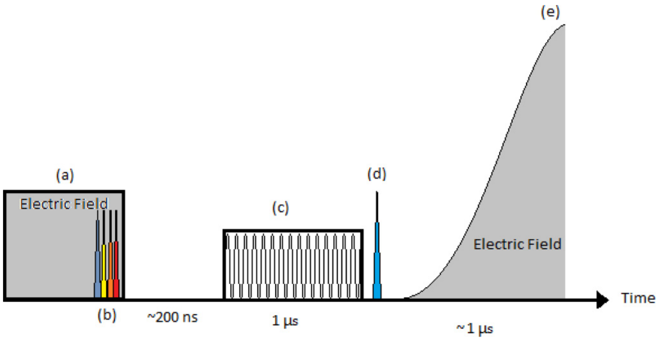

FIG. 5. (Color online) The timing sequence for the lasers, microwaves, and rf signals. (a) Small electric field to clear photoions. (b) Four laser pulses to drive the $6s^2 \rightarrow 6sng$ transition. (c) 1 μs microwave pulse. (d) ICE laser pulse (e) Electric field ramp.

IV. EXPERIMENTAL OBSERVATIONS

A. One-photon intervals

To obtain the single-photon intervals, we started from the known $6s18g$-$6s18h$ transition. We used a high microwave power at the $6s18g$-$6s18h$ resonance to equilibrate the populations, and we swept the diode laser frequency to find the frequency of the $6s18h \rightarrow 6p_{1/2}18h$ ICE transition. With the laser set to the ICE frequency we then attenuated the microwave power and scanned the microwave frequency to repeat the earlier measurements. To find the $6sng$-$6snh$ transitions of $n < 18$, we changed the diode laser frequency from its $n = 18$ value using Eq. (3) and scanned the microwave frequency at high power to find a small resonance signal. We then optimized the signal by adjusting the diode laser frequency with the microwave frequency set to the $6sng$-$6snh$ frequency. Once we found the optimal diode laser frequency, we performed our microwave scans at reduced microwave power.

Typical resonances, for $n = 15$, are shown in Fig. 6. There are two resonances, corresponding to the two possible values of K for the $6s15h$ state. The one-photon transition frequencies for $6sng$ to $6snh$, $15 \leqslant n \leqslant 18$, are shown in Table I.

TABLE I. ng-nh observed frequencies and K splittings.

n	$K = 9/2$ (MHz)	$K = 11/2$ (MHz)	K splitting (MHz)
18	40180.0(6)	41147.4(7)	967.4(9)
17	47367.4(6)	48547.2(6)	1179.8(8)
16	56489.4(6)	57959.0(5)	1469.6(8)
15	68185.8(5)	70063.6(5)	1877.8(7)

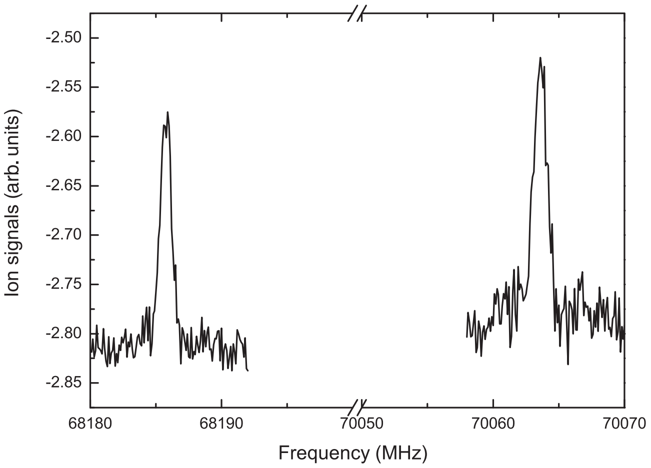

FIG. 6. The single-photon $6s15g \rightarrow 6s15h$ transitions. The two peaks are separated by the K splitting.

B. Two-photon intervals

The procedure used for the two-photon transitions from $6sng$ to $6sni$ was similar to that used for the one-photon transitions. Using the known $6s18g$-$6s18i$ transition frequencies we found the ICE wavelength for $6s18i$, which could then be adjusted for lower n using Eq. (3). The two-photon $6sng$-$6sni$ transition occurs via a virtual intermediate state, and there is a small but measurable ac Stark shift due to the microwave field. To obtain the unshifted intervals, we took measurements at multiple microwave powers and extrapolated our results to zero microwave power. With the available microwave power the maximum ac Stark shift was 1.65 MHz. The uncertainties are those given by the statistical fits to the power extrapolations. Typical two-photon resonances, for $n = 15$, are shown in Fig. 7. The two-photon transition frequencies for $6sng$ to $6sni$, $15 \leqslant n \leqslant 18$ are shown in Table II.

TABLE II. ng-ni observed intervals and K splittings.

n	$K = 11/2$ (MHz)	$K = 13/2$ (MHz)	K splitting (MHz)
18	51422.9(3)	51654.6(3)	231.7(4)
17	60667.8(6)	60926.7(8)	258.9(10)
16	72375.6(3)	72669.2(3)	293.6(4)
15	87359.8(4)	87691.3(3)	331.5(5)

C. Three-photon intervals

We located the $6snk \rightarrow 6p_{1/2}nk$ ICE transitions in essentially the same manner used to find the $6snh \rightarrow 6p_{1/2}nh$ and $6sni \rightarrow 6p_{1/2}ni$ ICE transitions. We do not have enough microwave power to drive the three-photon $6sng$-$6snk$ transitions using a single microwave field. Instead, we use two frequencies. One is close to the two-photon $6sng$-$6sni$ microwave frequency, and the other is close to the $6sni$-$6snk$ frequency, which, for clarity, we term a radio frequency (rf), even though it can be as high as 8.3 GHz. In all cases, the rf frequency was fixed and the microwave frequency swept. We verified that if we changed the rf frequency the $6sng$-$6snk$ intervals were given by twice the microwave frequency plus the rf frequency, indicating that the resonance was due to two microwave photons and one rf photon.

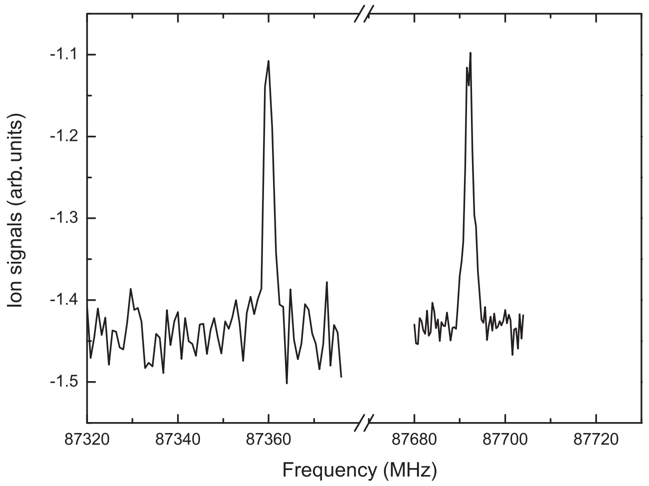

FIG. 7. The two-photon transitions $6s15g \rightarrow 6s15i$. The two resonances are separated by the K splitting of the $6s15i$ state.

There are now two ac Stark shifts, due to the microwave and rf fields. We performed microwave frequency sweeps at different microwave powers and constant rf power, allowing us to extrapolate the observed resonance frequencies to zero microwave power for a given rf power. We repeated this procedure for several different rf powers to extrapolate to zero microwave and rf power. Our fit for the $6s17g \rightarrow 6s17k$, $K = 15/2$, transition is shown in Fig. 8. As expected, the rf power shift is more important since the rf field is nearly resonant with a one-photon transition. In Table III we give the measured intervals after extrapolation, as well as the approximate microwave and rf frequencies used. The uncertainties in our reported intervals correspond to the uncertainties of the power extrapolations.

V. CORE POLARIZATION ANALYSIS OF THE DATA

The adiabatic core polarization model of Mayer and Mayer provides an instructive starting point for the analysis. In it, the energy by which a Ba $6sn\ell$ Rydberg state lies below the hydrogenic energy of $-1/2n^2$ is given by [5]

$$W_{\mathrm{pol},n\ell} = -\tfrac{1}{2}\alpha_d \langle r^{-4}\rangle_{n\ell} - \tfrac{1}{2}\alpha_q \langle r^{-6}\rangle_{n\ell}, \tag{5}$$

where α_d and α_q are the dipole and quadrupole polarizabilities of the Ba^+ ionic core, and $\langle r^{-4}\rangle_{n\ell}$ and $\langle r^{-6}\rangle_{n\ell}$ are the expectation values of the squares of the $n\ell$ Rydberg electron's field and field gradient at the core. The model is termed adiabatic because it is based on the assumption that the Rydberg electron is slowly moving compared to the electrons in the core, providing an essentially static field.

For comparison to experimental data, it is convenient to use Edlen's form of Eq. (5) [7]:

$$W_{\mathrm{pol},n\ell} = -\alpha_d P_{n\ell} - \alpha_q P_{n\ell} Q_{n\ell}, \tag{6}$$

where

$$P_{n\ell} = R\langle r^{-4}\rangle_{n\ell}, \tag{7}$$

$$Q_{n\ell} = \frac{\langle r^{-6}\rangle_{n\ell}}{\langle r^{-4}\rangle_{n\ell}}, \tag{8}$$

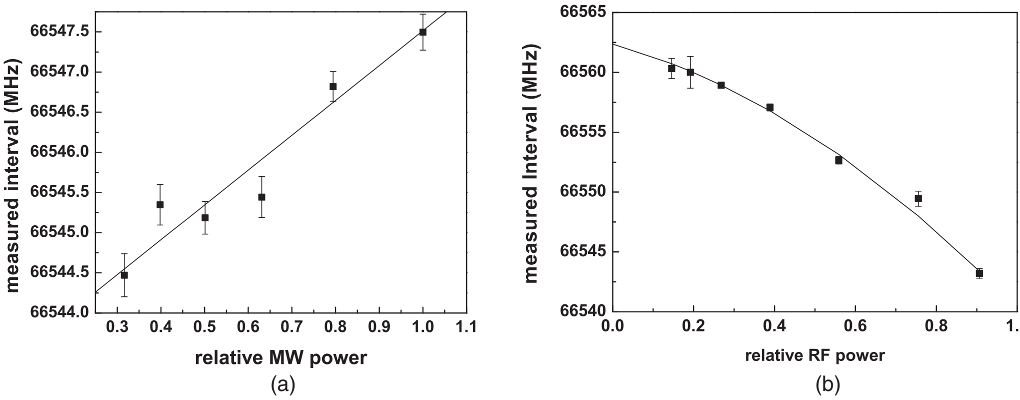

FIG. 8. The extrapolation of the three-photon $6s17g \rightarrow 6s17k$, $K = 15/2$, transition to zero power. (a) Resonances were recorded for multiple microwave powers at each rf power to determine the zero-microwave-power resonance frequency for each rf power. (b) These zero-microwave-power frequencies were then extrapolated to find the zero-power interval, assuming a linear plus quadratic rf power shift, as shown.

and R is the Rydberg constant for Ba; $R = 109\,736.88\ \text{cm}^{-1}$. Experimentally, we observe the $\Delta\ell$ energy intervals $\Delta W_{\text{pol},n\ell'\ell} = W_{\text{pol},n\ell'} - W_{\text{pol},n\ell}$ between Ba $6sn\ell$ and $6sn\ell'$ states of the same n, and we can express the observed intervals in terms of Eq. (6) using

$$\frac{\Delta W_{\text{pol},n\ell'\ell}}{\Delta P_{n\ell\ell'}} = \alpha_d + \alpha_q \frac{\Delta PQ_{n\ell\ell'}}{\Delta P_{n\ell\ell'}}. \tag{9}$$

Here $\Delta P_{n\ell\ell'} = P_{n\ell} - P_{n\ell'}$, and $\Delta PQ_{n\ell\ell'} = P_{n\ell}Q_{n\ell} - P_{n\ell'}Q_{n\ell'}$. The $\Delta\ell$ intervals are largely determined by the dipole polarizability, and in Eq. (9) we have removed the variation due to the dipole polarizability by dividing by $\Delta P_{n\ell\ell'}$. Plotting the left-hand side of Eq. (9) vs $\Delta PQ_{n\ell\ell'}/\Delta P_{n\ell\ell'}$ yields a graph with intercept α_d and slope α_q. In Fig. 9, we have plotted Eq. (9) for the Ba $6sn\ell$ $\ell \rightarrow \ell + 1$ intervals of $\ell \geqslant 5$. The experimental intervals are taken from Gallagher *et al.* [10], Snow and Lundeen [12], and this work. The $\ell \rightarrow \ell + 1$ intervals of $\ell > 6$, $n = 17$ and 20, the high-ℓ intervals, at $\Delta PQ_{n\ell\ell'}/\Delta P_{n\ell\ell'} < 0.002$ fall on a line, as expected, but the $\ell = 6 \rightarrow \ell = 7$, *ni*-*nk*, intervals at $\Delta PQ_{n\ell\ell'}/\Delta P_{n\ell\ell'} \approx 0.0025$ lie distinctly above the line, and the $\ell = 5 \rightarrow \ell = 6$, *nh*-*ni*, intervals, at $\Delta PQ_{n\ell\ell'}/\Delta P_{n\ell\ell'} \approx 0.0053$, lie well below the line. The latter two sets of data are displaced from the line due to the breakdown of the adiabatic assumption implicit in Eq. (5).

Almost immediately after the appearance of the paper by Mayer and Mayer, van Vleck and Whitelaw [6] pointed out that Eq. (5) is valid only in the limiting case in which the excited states of the ionic core are far above its ground state. Furthermore, the polarization shifts are are not first-order shifts, as implied by Eq. (5), but second-order shifts. To understand their approach, it is useful to think of the Ba atom as consisting of an inert, but polarizable, Ba^{++} core and two valence electrons. In this case the dipole and quadrupole polarization shifts of the $6sn\ell$ state are due to the dipole and quadrupole couplings of the $6sn\ell$ state to the doubly excited $NLn\ell'$ states. Here NL is the state of Ba^+, and $n\ell'$ is the state of the Rydberg electron. The energy shifts are readily calculated in second-order perturbation theory by summing the contributions of all the coupled $NLn\ell'$ states, including continua. For example, the quadrupole polarization energy of the Ba $6s20i$ state comes from the quadrupole couplings to doubly excited Ba $Ndn\ell'$ states with $\ell' = 4, 6,$ and 8, as shown schematically in Fig. 10. Summing over all the coupled $Ndn\ell'$ states yields the quadrupole polarization shift. As shown in Fig. 10 for the specific case of $N = 6$, Δ is the energy range spanned by the $n\ell'$ states associated with an Nd ion state, and Ω is the energy difference between the Ba^+ $6s$ and Nd states. If $\Delta \ll \Omega$ for all N, the sum reduces to $\alpha_q\langle r^{-6}\rangle_{20i}/2$, as in Eq. (5). Thus, a more precise statement of the adiabatic requirement is $\Delta \ll \Omega$ for all NL. For the Ba $Ndn\ell'$ states of

TABLE III. *ng*-*nk* frequencies and intervals.

n	K	Approximate rf frequency (MHz)	Approximate microwave frequency (MHz)	Extrapolated interval (MHz)
18	13/2	4920	25750	56388.0(20)
	15/2	4640	25895	56424.5(30)
17	13/2	5750	30390	66521.1(12)
	15/2	5750	30400	66562.4(17)
16	13/2	7050	36125	79351.4(17)
	15/2	7050	36150	79393.0(20)
15	13/2	8300	43720	95739.1(20)
	15/2	8100	43875	95798.9(20)

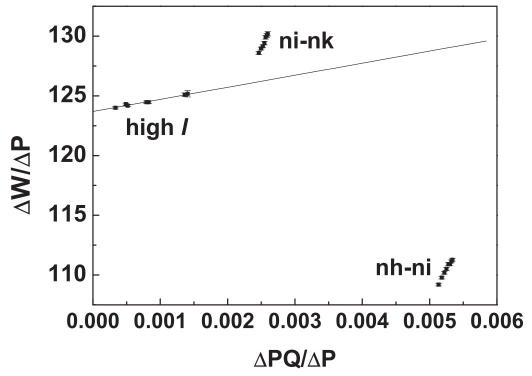

FIG. 9. The adiabatic plot of the measured $\Delta\ell$ intervals using Eq. (9).

$N > 5$ the adiabatic requirement is reasonably well satisfied, but for $N = 5$ it is not.

The most important quadrupole couplings by far are those between the $6sn\ell$ and $5dn'\ell'$ states. As an example we consider the $6s20i$ state, which is coupled to the $5dng$, $5dni$, and $5dn\ell$ states. These states are not energetically removed from the $6s20i$ state by the Ba$^+$ $6s$-$5d$ interval of $\sim$5000 cm^{-1}, as assumed in the adiabatic model, but by a range of energies comparable to the ion interval. In this case $\Delta \cong \Omega$, and the adiabatic model fails, as shown graphically in Fig. 9. Nonetheless, using hydrogenic wave functions it is straightforward to calculate the energy shift due to the quadrupole coupling to the $5dn\ell'$ states and compare it to that expected from the adiabatic model, yielding the ratio, or correction factor, k_q. Thus we can write the quadrupole polarization shift of the $6s20i$ states due to the $5dn\ell'$ states as $k_q\alpha_q'\langle r^{-6}\rangle_{20i}/2$, where α_q' is the part of the quadrupole polarizability due to the Ba$^+$ $5d$ state. An analogous procedure can be carried out for the dipole polarization shift, leading to the correction factor k_d. An important point to keep in mind is that k_d and k_q correct for the nonadiabatic effects in the dipole and quadrupole polarization energy shifts, respectively. They are not corrections to the polarizabilities. Thus, for example, the nonadiabatic effect in the dipole polarization energy affects both α_d and α_q.

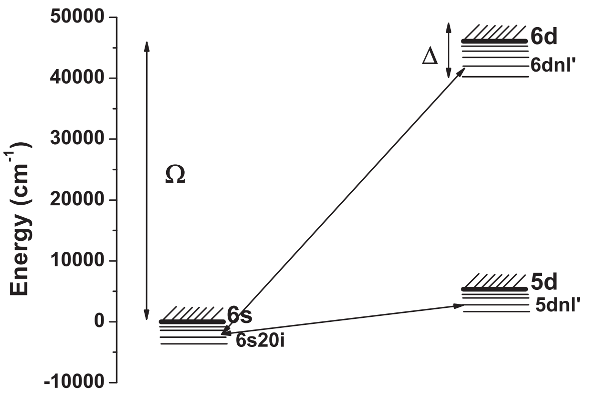

FIG. 10. Energy level diagram showing the quadrupole coupling of the $6s20i$ state to $Ndn\ell'$ states ($\ell' = 4$, 6, and 8). The Ba$^+$ $6s$ ground-state energy is set to zero. Δ is the energy spread of the $n\ell'$ states, and Ω is the $6s$-Nd ion energy spacing, shown here for $N = 6$. The adiabatic requirement $\Delta \ll \Omega$ is clearly not satisfied for $N = 5$.

With the realization that the polarization energy shifts are simply derived from second-order perturbation theory we can understand why the ni-nk and nh-ni intervals are displaced as they are in Fig. 9. A $6sni$ state has a very strong quadrupole interaction with the low-lying $5d5g$ state which is only $\sim$1000 cm^{-1} above the $6sni$ state. For this reason, the quadrupole polarization energy shift is greater than expected from the adiabatic model, and the ni-nk points lie above the line in Fig. 9. The nh-ni intervals lie below the line in Fig. 9 because the $6snh$ states have a strong quadrupole interaction with the $5d4f$ state which lies $\sim$1000 cm^{-1} below the $6s20h$ state. The quadrupole interaction shifts the $6s20h$ state up in energy, changing the sign of the quadrupole polarization shift.

The high-ℓ points in Fig. 9 at $\Delta PQ_{n\ell\ell'}/\Delta P_{n\ell\ell'} < 0.001$ fit a straight line fairly well, and we can extract values for α_d and α_q from the intercept and slope of the line through these points, which we term the apparent polarizabilities. The values we obtain are $\alpha_d^{\mathrm{app}} = 123.67(6)a_0^3$ and $\alpha_q^{\mathrm{app}} = 1047(63)a_0^5$. These values are too small, due to neglect of the nonadiabatic corrections, and for this reason we term the extracted values the apparent polarizabilities.

To extract the correct values of α_d and α_q for Ba$^+$ from the $\Delta\ell$ intervals of the Ba $6sn\ell$ states, we must account for the nonadiabatic effects, which are prominent in Fig. 9. There are several approaches, and we first describe our approach. We start by noting that the contributions to the Ba$^+$ $6s$ polarizabilities from Ba$^+$ states above the $6p$ and $5d$ states are essentially adiabatic, as are those from Ba^{2+}. We assume the nonadiabatic effects to arise only from the $6p$ and $5d$ states of Ba$^+$, as done by Snow and Lundeen [13]. Accordingly, we write the analog to Eq. (5) as

$$W_{\mathrm{pol},n\ell} = -\tfrac{1}{2}(\alpha_d'k_d + \alpha_d'')\langle r^{-4}\rangle_{n\ell} - \tfrac{1}{2}(\alpha_q'k_q + \alpha_q'')\langle r^{-6}\rangle_{n\ell}, \tag{10}$$

where α_d' is the part of the dipole polarizability due to the $6p$ state of the Ba$^+$ ion, α_q' is the part of the quadrupole polarizability due to the $5d$ state of the Ba$^+$ ion, α_d'' is the part of the dipole polarizability due to the higher-p states of the Ba$^+$ ion and the dipole polarizability of Ba^{2+}, and α_q'' is the part of the quadrupole polarizability due to the higher-d states of the Ba$^+$ ion and the quadrupole polarizability of Ba^{2+}. The nonadiabatic effects are taken into account by introducing the correction factors k_d and k_q [10,13]. In principle, the k_d and k_q factors completely eliminate the nonadiabatic effects. It is straightforward to calculate k_d and k_q if we assume the outer electron to be hydrogenic. Our calculated values of k_d are given in Table IV, and to three significant digits there is no n dependence. The n-dependent k_q values are presented in Table V.

If we define the quantities $P_{n\ell}'$ and $Q_{n\ell}'$ as follows:

$$P_{n\ell}' = k_d P_{n\ell} \tag{11}$$

and

$$Q_{n\ell}' = \frac{k_q}{k_d} Q_{n\ell}, \tag{12}$$

TABLE IV. k_d calculated values.

n	$\ell = 5$	$\ell = 6$	$\ell = 7$	$\ell = 8$	$\ell = 9$	$\ell = 10$	$\ell = 11$
15	0.955278	0.969324	0.979127				
16	0.955326	0.969248	0.978992				
17	0.955494	0.969194	0.978904	0.984568	0.987537	0.989361	
18	0.955404	0.969168	0.978870				
19	0.955470	0.969141	0.978841				
20	0.955510	0.969136	0.978841	0.981743	0.984323	0.985240	0.987553
21	0.955543	0.969128	0.978847				
22	0.955584	0.969126					
23	0.955619						

the energy difference between the ℓ states of the same n can be written as

$$\Delta W_{\mathrm{pol},n\ell'\ell} = \alpha'_d \Delta P'_{n\ell\ell'} + \alpha''_d \Delta P_{n\ell\ell'} + \alpha'_q \Delta P'Q'_{n\ell\ell'} + \alpha''_q \Delta PQ_{n\ell\ell'}, \qquad (13)$$

where $\Delta W_{\mathrm{pol},n\ell'\ell}$, $\Delta P_{n\ell\ell'}$, and $\Delta PQ_{n\ell\ell'}$ are as defined earlier, $\Delta P'_{n\ell\ell'} = P'_{n\ell} - P'_{n\ell'}$ and $\Delta P'Q'_{n\ell\ell'} = P'_{n\ell}Q'_{n\ell} - P'_{n\ell'}Q'_{n\ell'}$. If we group the α''_d and α''_q terms with the observed energy intervals and divide Eq. (13) by $\Delta P'_{\ell\ell'}$, we obtain the following expression:

$$\frac{\Delta W_{\mathrm{pol},n\ell'\ell} - \alpha''_d \Delta P_{n\ell\ell'} - \alpha''_q \Delta PQ_{n\ell\ell'}}{\Delta P'_{n\ell\ell'}} = \alpha'_d + \alpha'_q \frac{\Delta P'Q'_{n\ell\ell'}}{\Delta P'_{n\ell\ell'}}, \qquad (14)$$

which is the nonadiabatic analog of Eq. (9).

If we know α''_d and α''_q, we can extract α'_d and α'_q from their linear relationship with the measured $\Delta\ell$ intervals, using the center of gravity of each $6sn\ell$ state. From Ref. [20], $\alpha''_d = 10.15(53)a_0^3$ and $\alpha''_q = 814(11)a_0^5$. Figure 11(a) shows the fit of the experimental data to Eq. (14) using our calculated $\Delta P_{n,\ell\ell'}$, $\Delta PQ_{n,\ell\ell'}$, $\Delta P'_{n,\ell\ell'}$, and $\Delta P'Q'_{n,\ell\ell'}$. In Fig. 11 and in all similar plots, for the nh-ni and ni-nk intervals n increases from 15 to 21 as $\Delta P'Q'/\Delta P'$ increases. Unlike in Fig. 9, the experimental data can be fitted reasonably well by a straight line, and from Fig. 11(a), we obtain $\alpha'_d = 114.47(7)a_0^3$ and $\alpha'_q = 1725(14)a_0^5$. While Fig. 11(a) is an enormous improvement over Fig. 9, the data clearly do not fit the model, as shown by the residuals in Fig. 11(b).

Due to the obvious systematic variations of the residuals, shown in Fig. 11(b), the uncertainties of the values of α'_d and α'_q are larger than the uncertainties from the fit. To understand these uncertainties we have fitted the data in other ways. The first is to remove the lower-ℓ intervals, which have larger nonadiabatic corrections, from the fit. In Fig. 12(a) we show the fit obtained by removing the nh-ni intervals from Fig. 11(a). The resulting values, $\alpha'_d = 114.66(12)a_0^3$ and $\alpha'_q = 1664(36)a_0^5$, are not very different from those extracted from Fig. 11(a). The residuals are shown in Fig. 12(b). There are several points to note about Fig. 12(b). First, we note that there is a discontinuity between $n = 18$ and $n = 19$ in the ni-nk points, which may be due to a perturbation of the energy levels, which we cannot hope to fit. Second, we believe the $n = 20$ $\ell = 7 \rightarrow \ell = 8$ and $\ell = 10 \rightarrow \ell = 11$ points to be in error. We shall return to this point. Finally, if the two $n = 20$ points and the discontinuity at $n = 18$ are ignored, the systematic variation of the residuals is essentially gone. If we remove the ni-nk intervals from Fig. 12(a), leaving only the high-ℓ intervals from Snow and Lundeen, we obtain the plot of Fig. 13, which yields $\alpha'_d = 115.08(16)a_0^3$ and $\alpha'_q = 1160(170)a_0^5$. With this restricted set of data the scatter is now clearly more important than any systematic variation. Inspection of the $\ell = 7 \rightarrow \ell = 8$ points of Fig. 13 shows why we believe the $n = 20$ points to be suspect. The two $\ell = 7 \rightarrow \ell = 8$ points by themselves imply an impossible negative quadrupole polarizability, as do the $\ell = 10 \rightarrow \ell = 11$ and either of the $\ell = 9 \rightarrow \ell = 10$ points.

TABLE V. k_q calculated values.

n	$\ell = 5$	$\ell = 6$	$\ell = 7$
15	−0.982	1.439	1.032
16	−0.889	1.473	1.039
17	−0.818	1.503	1.044
18	−0.761	1.531	1.050
19	−0.715	1.555	1.054
20	−0.678	1.577	1.058
21	−0.647	1.596	1.061
22	−0.620	1.614	
23	−0.598		

An alternative approach is to fit the $\Delta\ell$ intervals for each n state separately, and in Fig. 14 we show the values of α'_d and α'_q extracted from the data shown in Fig. 11(a). Only for $n = 17$ and 20 are there more than two $\Delta\ell$ intervals, so only in those two cases can we show uncertainties for the fits. We expect that if we had more points the uncertainties of the other n states would be similar. If we disregard the obvious outliers at $n = 18$ and 21, there is no monotonic increase or decrease in the value of α'_d, and the average value, $\alpha'_d = 114.51(2)a_0^3$, is similar to the value extracted from Fig. 11(a). The $n = 18$ intervals were measured in two different experiments, so we do not think the $n = 18$ points are displaced from the others due to an experimental problem, but for a physical reason. As already noted, the ni-nk residuals of Fig. 12(b) exhibit a discontinuity at $n = 18$, which might be a sign of a series perturbation. The $n = 21$ points in Fig. 14 probably reflect experimental error.

In contrast to the relatively constant values of α'_d shown in Fig. 14, the extracted values of α'_q show a clear n dependence, and we suspect that its origin lies in our calculation of k_q,

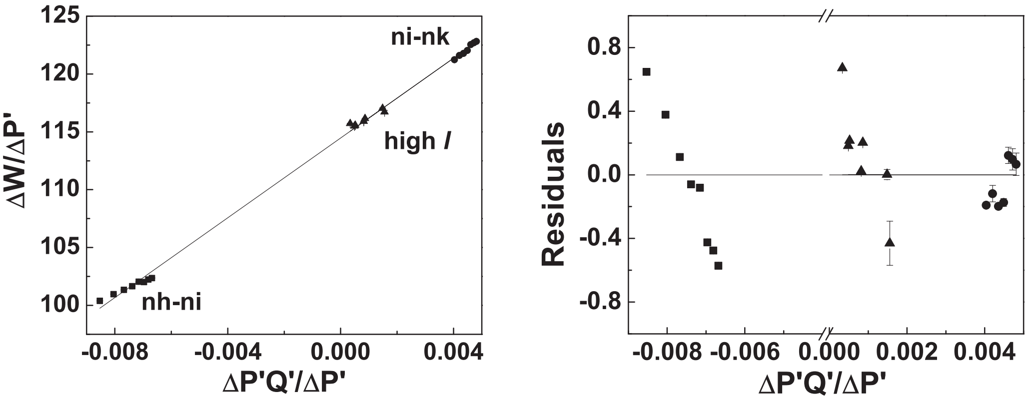

(a) (b)

FIG. 11. (a) Graph of $(\Delta W_{\text{pol},n\ell'\ell} - \alpha_d''\Delta P_{n\ell\ell'} - \alpha_q''\Delta PQ_{n\ell\ell'})/\Delta P'_{n\ell\ell'}$ vs $\Delta P'Q'_{n\ell\ell'}/\Delta P'_{n\ell\ell'}$. The symbols ■, ●, and ▲ are the data points presenting the *nh-ni*, *ni-nk*, and high-ℓ intervals, respectively. For the *nh-ni* and *ni-nk* intervals n increases monotonically from 15 to 21 as $\Delta P'Q'/\Delta P'$ increases. The high-ℓ intervals are for $n = 17$ and 20. The linear fit yields the y intercept and the slope, which are the values of α_d' and α_q', respectively. From the graph, we obtain $\alpha_d' = 114.47(7)a_0^3$ and $\alpha_q' = 1725(14)a_0^5$, and in (b) the plot displays the residuals relative to the fit, which is the zero line.

especially for $\ell = 5$. There are several sources of error in calculations of k_d and k_q. We have ignored the spin-orbit splittings of the Ba$^+$ $6p$ and $5d$ states, and we have assumed the outer electron to be hydrogenic. The latter assumption leads to incorrect energies, and, more important, incorrect wave functions. For this problem, matrix elements of inverse powers of r are required, which in turn requires wave functions accurate at small r. Unfortunately, there is no simple method to generate nonhydrogenic wave functions which are accurate at small r.

Irrespective of the source of the variation in α_q' seen in Fig. 14, it is clear that we cannot extract a value of α_q' from these data, and the value of α_d' is also suspect. Accordingly, we have fitted the *ni-nk* and higher-ℓ intervals of Fig. 12(a) for $n = 17$ and 20, the only n values for which we have more than one $\Delta\ell$ interval. For $n = 17$ we obtain $\alpha_d' = 114.62(5)a_0^3$ and $\alpha_q' = 1640(23)a_0^5$, and for $n = 20$ $\alpha_d' = 114.73(27)a_0^3$ and $\alpha_q' = 1650(120)a_0^5$. The $n = 17$ data lie almost perfectly on a straight line, while the $n = 20$ data are more scattered. The important point is that α_q' exhibits no n dependence. Thus we conclude that the fit of Fig. 12(a) provides the best values for α_d' and α_q'. The high-ℓ data shown in Fig. 13 exhibit no systematic problem, but the high-ℓ intervals are more susceptible to Stark shifts and are not as sensitive to the quadrupole polarizability as are the lower-ℓ intervals.

To account for possible systematic effects in the determination of α_d' and α_q' we increase their uncertainties from the fit shown in Fig. 12(a) to encompass the residuals shown in Fig. 12(b) except the two $n = 20$ points mentioned previously. The results are $\alpha_d' = 114.66(25)a_0^3$ and $\alpha_q' = 1664(50)$. Adding them to α_d'' and α_q'' we obtain the ionic Ba$^+$ dipole and quadrupole polarizabilities $\alpha_d = 124.81(25)a_0^3$ and $\alpha_q = 2478(50)a_0^5$, respectively.

It is useful to compare our values to those obtained from other measurements and theory. In Table VI we present the values obtained for α_d, and in Table VII, we present the values for α_q' and α_q. Our value for α_d agrees with the theoretical value to within the theoretical uncertainty, but our value for α_q is half the theoretical value. It is perhaps more interesting to compare the experimental results. Two methods have been

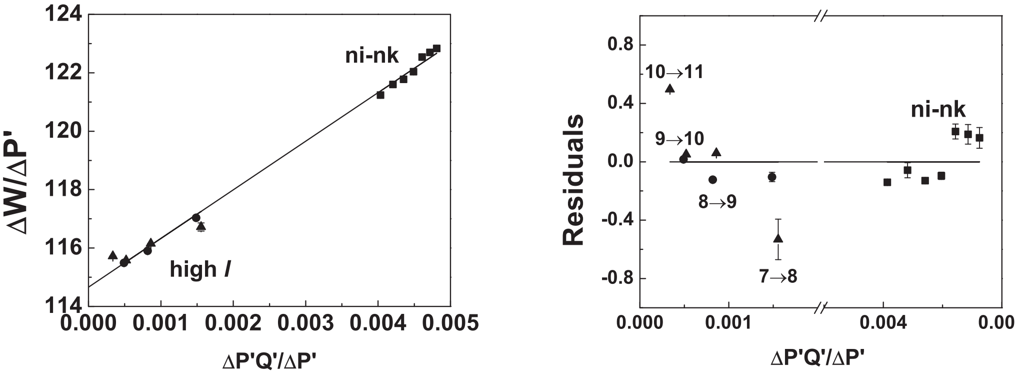

(a) (b)

FIG. 12. (a) Plot obtained by removing the *nh-ni* intervals from the data in Fig. 11(a). For the *ni-nk* intervals n increases monotonically from 15 to 21 as $\Delta P'Q'/\Delta P'$ increases. The high-ℓ points are for $n = 17$ (●) and $n = 20$ (▲). From the graph, we obtain $\alpha_d' = 114.66(12)a_0^3$ and $\alpha_q' = 1664(36)a_0^5$. (b) The residuals of (a). There is far less systematic variation of the residuals than in Fig. 11(b).

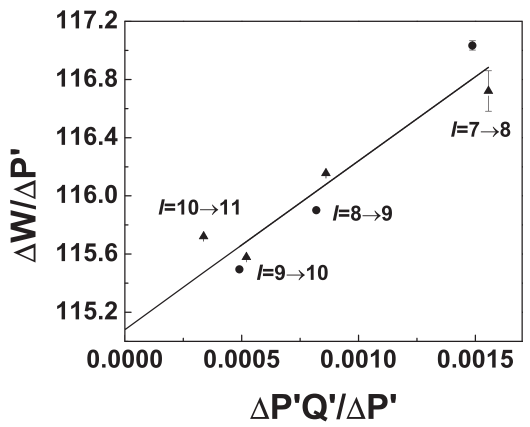

FIG. 13. Plot of high-ℓ intervals from Fig. 11(a) for $n = 17$ (●) and $n = 20$ (▲). From the graph, we obtain $\alpha'_d = 115.08(16)a_0^3$ and $\alpha'_q = 1160(170)a_0^5$.

TABLE VI. The Ba$^+$ $6s$ dipole polarizability (α_d) obtained from this work, and other theoretical and experimental results.

	α_d (units of a_0^3)
Core polarization	
This work	124.81(25)
Expt. [10]	125.5(10)
Expt. [13]	124.30(16)
Expt. [21]	123.88(5)
K splitting	
Expt. [16]	121.3(66)
Expt. [22]	123.88(5)
Theory [20]	124.15

used to extract the polarizabilities, polarization analysis of the $\Delta\ell$ intervals and analysis of the K splittings. Analysis of the K splittings yields the Ba$^+$ $6s$-$6p$ and $6s$-$5d$ radial matrix elements, from which α'_d and α'_q are easily computed. To the values of α'_d and α'_q given in Ref. [16] we have added the theoretical values $\alpha''_d = 10.15a_0^3$ and $\alpha''_q = 814a_0^5$ yielding the values of α_d and α_q given in Tables VI and VII. While it is possible to make good measurements of the K splittings, they arise completely from the nonadiabatic effects, and their analysis is much more complicated than a polarization analysis of $\Delta\ell$ intervals. For this reason, we choose to compare our results to those of Snow and Lundeen, Ref. [21].

Using essentially the same data as we have used here, Snow and Lundeen [21] arrived at a value of α_d distinctly smaller than ours and a value of α_q almost twice ours. To understand the origin of the differences it is useful to use four different methods to analyze the data. Specifically, we consider ignoring the nonadiabatic effects, using the adiabatic expansion method, introducing k_q and using the adiabatic expansion method to account for nonadiabatic effects in the dipole polarization energy, and finally introducing both k_q and k_d. For simplicity, we label these methods I, II, III, and IV, respectively. Method III is similar to that used by Snow and Lundeen, and IV is similar to ours.

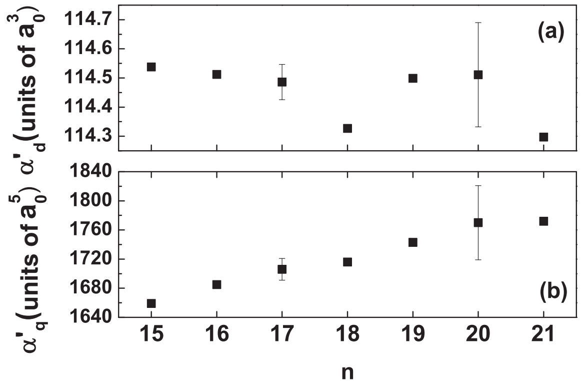

FIG. 14. Graph showing the values of (a) α'_d and (b) α'_q extracted from $\Delta\ell$ intervals for each n. Disregarding the obvious outliers at $n = 18$ and 21, there is no monotonic increase or decrease in the value of α'_d, and the average value is $\alpha'_d = 114.51(2)a_0^3$. A value of α'_q cannot be extracted from (b). Only $n = 17$ and 20 have more than two data points (the nh-ni, ni-nk, and high-ℓ intervals), and therefore only their uncertainties can be shown.

If we restrict our attention to only the high-ℓ intervals, it is not unreasonable to think that the data can be fitted by ignoring the nonadiabatic effects, method I, and using Eq. (9). The straight line through the high-ℓ points of Fig. 9 is precisely this fit. It yields $\alpha_d = \alpha_d^{\mathrm{app}} = 123.67a_0^3$ and $\alpha_q = \alpha_q^{\mathrm{app}} = 1047a_0^5$.

In the adiabatic expansion method, method II, the polarization energy of Eq. (5) is replaced by

$$W_{\mathrm{pol},n\ell} = -\tfrac{1}{2}\alpha_d\langle r^{-4}\rangle_{n\ell} - \tfrac{1}{2}(\alpha_q - 6\beta_1)\langle r^{-6}\rangle_{n\ell}\cdots, \qquad (15)$$

where the ellipsis indicates terms containing expectation values of higher inverse powers of r. The most important difference, from our present point of view, is the presence of $6\beta_1$ in the $\langle r^{-6}\rangle$ term, which is due to the nonadiabatic effect in the dipole polarization energy. It appears in the same way as the quadrupole polarizability, and for Ba $\beta_1 = 605(25)a_0^5$ [21]. The higher inverse powers of r represent higher-order terms due to the nonadiabatic effect in the dipole polarization energy, the nonadiabatic effect in the quadrupole polarization energy, and higher multipole terms. As Snow and Lundeen have shown, these terms can be represented by higher-order terms in $\langle r^{-6}\rangle/\langle r^{-4}\rangle$, or equivalently, in $\Delta PQ/\Delta P$, so that the data points of Fig. 9 no longer need to be fitted by a straight line. Application of the adiabatic expansion method is based on the assumption that the expansion is convergent. Inspection of Fig. 9 suggests that very high-order terms in $\Delta PQ/\Delta P$ will be

TABLE VII. The Ba$^+$ $6s$ quadrupole polarizability (α_q) and the contribution of the Ba$^+$ $5d$ state (α'_q) to it.

	α'_q (units of a_0^5)	α_q (units of a_0^5)
Core polarization		
This work	1664(50)	2478(50)
Expt. [10]		2050(100)
Expt. [21]	1524(8)	4420(250)
Expt. [13]	1828(88)	2462(361)
K splitting		
Expt. [16]	1562(93)	2376(93)
Expt. [22]	3606(250)	4420(250)
Theory [20]	3368(34)	4182(34)

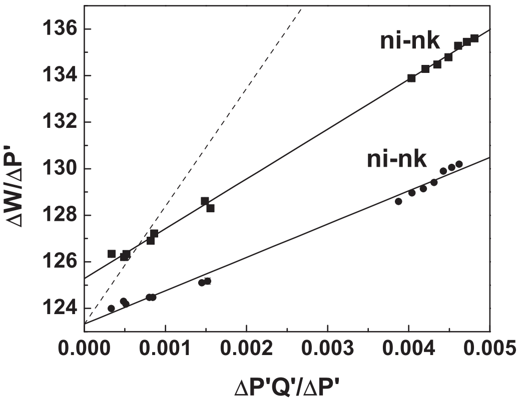

FIG. 15. Comparison between the use of method III to treat the *ni*-*nk* and the high-ℓ intervals (●) and method IV to treat the intervals (■). Here we assume that α''_d and α''_q both vanish. The introduction of k_q in method III removes the nonadiabatic effect in the quadrupole polarization energy, and all the data points fall on a line, unlike the plot of Fig. 9. The intercept of the fit line gives $\alpha_d = 123.33(11)a_0^3$. Adding $6\beta_1$ from the nonadiabatic correction to the dipole polarization energy to the slope of the fit line give the broken line, which has slope $\alpha_q = 5060a_0^5$. The introduction of k_d as well as k_q in method IV both raises the points and increases the slope of the fit line; the resulting intercept and slope are $\alpha_d = 125.28(8)a_0^3$ and $\alpha_q = 2138(24)a_0^5$.

TABLE VIII. The Ba$^+$ 6*s* dipole (α_d) and quadrupole polarizabilities (α_q) extracted from different methods of data analysis.

Analysis method	α_d (units of a_0^3)	α_q (units of a_0^5)
Method I: ignore nonadiabatic	123.67(6)	1047(63)
Method II: adiabatic expansion	123.67(6)	4680(160)
Method III: k_q and adiabatic expansion	123.33(11)	5060(150)
Method IV: k_d and k_q	125.28(8)	2138(23)
Snow and Lundeen [21]	123.88(5)	4420(250)
This work	124.81(25)	2478(50)

required to fit the data, indicating that the adiabatic expansion is almost certainly not convergent in this case. However, it should be applicable if we again restrict our attention to the high-ℓ states. Fitting the high-ℓ data of Fig. 9 to the first two terms of Eq. (15) leads to $\alpha_d = \alpha_d^{\mathrm{app}} = 123.67a_0^3$ and $\alpha_q = \alpha_q^{\mathrm{app}} + 6\beta_1 = 4677a_0^5$.

The deviation of the factors k_d and k_q from unity is an indication of the severity of the nonadiabatic effects. Inspection of Tables IV and V shows that $0.955 < k_d < 0.990$ while k_q ranges from -0.0982 to 1.614, suggesting that the nonadiabatic effect in the quadrupole polarization energy is by far the worse problem. Accordingly, we treat the data using method III, treating the nonadiabatic effects in the quadrupole and dipole polarization energies by k_q and an adiabatic expansion, respectively. This approach is approximately that used by Snow and Lundeen. It differs in that Snow and Lundeen, and we as well, separated the polarizabilities into two parts, for example, $\alpha_q = \alpha'_q + \alpha''_q$. To display most clearly the effect of introducing first k_q and then k_d we here assume that α''_d and α''_q both vanish, so that $\alpha'_d = \alpha_d$ and $\alpha'_q = \alpha_q$. Since $\alpha'_d = 0.92\alpha_d$, this approximation is excellent for α_d, and it is not unreasonable for α_q. In Fig. 15 using solid circles (●) we use method III to plot the high-ℓ and *ni*-*nk* intervals using the values of k_q given in Table V. Since we are now introducing k_q, and later shall introduce k_d, as the horizontal and vertical axes, we use $\Delta P' Q'_{n\ell'\ell}/\Delta P'_{n\ell\ell}$ and $\Delta W_{\mathrm{pol},n\ell'\ell}/\Delta P'_{n\ell\ell'}$. From the definitions of P' and Q' it is evident that P and Q are simply the special cases of P' and Q' for $k_d = k_q = 1$. The dominant effect of the introduction of k_q is to move points horizontally on the plot, which removes the glaring problem due to the nonadiabatic effects, the seemingly random distribution of points in Fig. 9. Now in Fig. 15 the solid circles (●) all lie along a straight line. In method III the adiabatic expansion needs to account only for the nonadiabatic effect on the dipole polarization. Accordingly, we fit the solid circles (●) to

$$\frac{\Delta W_{\mathrm{pol},n\ell'\ell}}{\Delta P'_{n\ell\ell'}} = \alpha_d + (\alpha_q - 6\beta_1)\frac{\Delta P' Q'_{n\ell\ell'}}{\Delta P'_{n\ell\ell'}}. \qquad (16)$$

The intercept of the fit line is $\alpha_d = 123.33(11)a_0^3$, and the slope $s_q = 1430(35)a_0^5$. The quadrupole polarizability $\alpha_q = s_q + 6\beta_1 = 5060a_0^5$ is the slope of the broken line in Fig. 15.

To show the effect of using k_d as well as k_q, method IV, in Fig. 15 we also plot, as solid squares (■), the high-ℓ and *ni*-*nk* intervals. The introduction of k_d has two effects, both of which are evident in Fig. 15. First, it raises all the points by 1%–3%, since $k_d < 1$ and $\Delta P' < \Delta P$. The effect is to raise the value of α_d; $\alpha_d = 125.28(8)a_0^3$. Second, since k_d falls further below 1 as ℓ is decreased, the slope of the line through the points is increased. In this method the slope (of the line through the square points) is $\alpha_q = 2138(23)a_0^5$. The nonadiabatic effect in the dipole polarization energy on α_q is the difference between the slopes of the lines through the squares and circles in Fig. 15, $708a_0^5$, much less than $6\beta_1 = 3630a_0^5$.

In Table VIII we have collected the results from the four analyses and presented them together with the values of Snow and Lundeen and ourselves. Methods I, II, and III yield essentially the same value of α_d, which implies that the adiabatic expansion method, or a modification which does not introduce k_d, has almost no effect on the value of α_d extracted. These values are also very close to the value obtained by Snow and Lundeen. The introduction of k_d, in method IV, vertically displaces the points in Fig. 15 and increases the value of α_d extracted to very nearly match our value. The quadrupole polarizabilities extracted by methods II and III are both much larger than those obtained by methods I and IV, due to the inclusion of $6\beta_1$ in the extracted value. These values are close to the value obtained by Snow and Lundeen. Method IV yields a value of α_q similar to our value and much smaller than those of methods II and III. From Table VIII it is evident that the difference between the values of both α_d and α_q extracted by Snow and Lundeen and ourselves is due almost entirely to the treatment of the nonadiabatic effect in the dipole polarization.

VI. CONCLUSION

We have demonstrated that ICE laser excitation to autoionizing states can be used to detect microwave transitions between high-angular-momentum Rydberg states of alkaline-earth-metal atoms, even though the ICE transitions are badly overlapped. We have used this technique to measure $\Delta\ell$ intervals between Ba $6sn\ell$ states of $15 \leqslant n \leqslant 18$ and $5 \leqslant \ell \leqslant 7$. Combining these measurements with other measurements of Ba $\Delta\ell$ intervals, we have extracted the Ba$^+$ polarizabilities $\alpha_d = 124.81(25)a_0^3$ and $\alpha_q = 2478(50)a_0^5$. These values disagree with recently reported experimental values due to the difference in the treatment of the nonadiabatic effects. In principle, the model we have used exactly accounts for the nonadiabatic effects by the introduction of the correction factors k_d and k_q, which are calculated numerically. The calculations can be improved by better numerical techniques, the inclusion of spin-orbit coupling, and the use of nonhydrogenic wave functions where required. We hope this work will stimulate theoretical activity along these lines.

ACKNOWLEDGMENTS

This work has been supported by the U.S. Department of Energy, Office of Basic Energy Sciences. J.N. would like to thank the Thailand Research Fund (TRF) and the National Research University Project under the Office of the Higher Education Commission (CHE), Ministry of Education Grant (Grant No. MRG5680117) for its support. We are grateful to S. R. Lundeen for helpful discussions.

---

[1] M. Chwalla, J. Benhelm, K. Kim, G. Kirchmair, T. Monz, M. Riebe, P. Schindler, A. S. Villar, W. Hänsel, C. F. Roos, R. Blatt, M. Abgrall, G. Santarelli, G. D. Rovera, and Ph. Laurent, Phys. Rev. Lett. **102**, 023002 (2009).
[2] N. Huntemann, M. Okhapkin, B. Lipphardt, S. Weyers, Chr. Tamm, and E. Peik, Phys. Rev. Lett. **108**, 090801 (2012).
[3] B. Arora, M. S. Safronova, and C. W. Clark, Phys. Rev. A **76**, 064501 (2007).
[4] U. I. Safronova and M. S. Safronova, Phys. Rev. A **79**, 022512 (2009).
[5] J. E. Mayer and M. G. Mayer, Phys. Rev. **43**, 605 (1933).
[6] J. H. Van Vleck and N. G. Whitelaw, Phys. Rev. **44**, 551 (1933).
[7] B. Edlen, *Handbuch der Physik* (Springer, Berlin, 1964).
[8] S. R. Lundeen, Adv. At., Mol. Opt. Phys. **52**, 161 (2005).
[9] T. R. Gentile, B. J. Hughey, D. Kleppner, and T. W. Ducas, Phys. Rev. A **42**, 440 (1990).
[10] T. F. Gallagher, R. Kachru, and N. H. Tran, Phys. Rev. A **26**, 2611 (1982).
[11] J. Nunkaew, E. S. Shuman, and T. F. Gallagher, Phys. Rev. A **79**, 054501 (2009).
[12] E. L. Snow and S. R. Lundeen, Phys. Rev. A **77**, 052501 (2008).
[13] E. L. Snow, M. A. Gearba, R. A. Komara, S. R. Lundeen, and W. G. Sturrus, Phys. Rev. A **71**, 022510 (2005).
[14] W. E. Cooke, T. F. Gallagher, S. A. Edelstein, and R. M. Hill, Phys. Rev. Lett. **40**, 178 (1978).
[15] E. L. Snow, R. A. Komara, M. A. Gearba, and S. R. Lundeen, Phys. Rev. A **68**, 022510 (2003).
[16] E. S. Shuman and T. F. Gallagher, Phys. Rev. A **74**, 022502 (2006).
[17] W. E. Cooke and T. F. Gallagher, Opt. Lett. **4**, 173 (1979).
[18] J. Nunkaew and T. F. Gallagher, Phys. Rev. A **81**, 023417 (2010).
[19] R. R. Jones and T. F. Gallagher, Phys. Rev. A **38**, 2846 (1988).
[20] E. Iskrenova-Tchoukova and M. S. Safronova, Phys. Rev. A **78**, 012508 (2008).
[21] E. L. Snow and S. R. Lundeen, Phys. Rev. A **76**, 052505 (2007).
[22] Shannon L. Woods, S. R. Lundeen, and Erica L. Snow, Phys. Rev. A **80**, 042516 (2009).